Assimilating Morning, Evening, and Nighttime Greenhouse Gas Observations in Atmospheric Inversions

V. C. Monteiro[1,2], J. C. Turnbull[1,3], N. L. Miles[4], K. J. Davis[4], Z. Barkley[4], A. Deng[5]

[1]GNS Science, Lower Hutt, New Zealand.

[2]Victoria University of Wellington, Wellington, New Zealand.

[3]University of Colorado at Boulder, Boulder, Colorado, USA.

[4]The Pennsylvania State University, University Park, Pennsylvania, USA.

[5]Vestas-American Wind Technology, Inc.

Corresponding author: Vanessa Monteiro (v.monteiro@gns.cri.nz)

Key Points:

- Assimilating non-afternoon greenhouse gas observations in atmospheric inversions is reliable when wind speeds are greater than 5m/s.
- Inclusion of non-afternoon atmospheric observations during windy conditions doubles the current data assimilation in atmospheric inversions.
- Additional observations in atmospheric inversions have the potential to improve greenhouse gas emissions estimates.

Abstract

Improved urban greenhouse gas (GHG) flux estimates are crucial for informing policy and mitigation efforts. Atmospheric inversion modelling (AIM) is a widely used technique combining atmospheric measurements of trace gas, meteorological modelling, and a prior emission map to infer fluxes. Traditionally, AIM relies on mid-afternoon observations due to the well-represented atmospheric boundary layer in meteorological models. However, confining flux assessement to daytime observations is problematic for the urban scale, where air masses typically move over a city in a few hours and AIM therefore cannot provide improved constraints on emissions over the full diurnal cycle. We hypothesized that there are atmospheric conditions beyond the mid-afternoon under which meteorological models also perform well. We tested this hypothesis using tower-based measurements of CO_2 and CH_4, wind speed observations, weather model outputs from INFLUX (Indianapolis Flux Experiment), and a prior emissions map. By categorizing trace gas vertical gradients according to wind speed classes and identifying when the meteorological model satisfactorily simulates boundary layer depth (BLD), we found that non-afternoon observations can be assimilated when wind speed is >5 m/s. This condition resulted in small modeled BLD biases (<40%) when compared to calmer conditions (>100%). For Indianapolis, 37% of the GHG measurements meet this wind speed criterion, almost tripling the observations retained for AIM. Similar results are expected for windy cities like Auckland, Melbourne, and Boston, potentially allowing AIM to assimilate up to 60% the total (24-h) observations. Incorporating these observations in AIMs should yield a more diurnally comprehensive evaluation of urban GHG emissions.

Plain Language Summary

It is crucial to improve greenhouse gas (GHG) emission estimates to inform policy and mitigation strategies. However, the current model techniques used to estimate such emissions rely on incorporating only mid-afternoon observations of atmospheric concentrations of GHGs. For cities, this limits a detailed understanding of emissions during hours of the day when emissions are the highest, such as the morning rush hours. This constraint is due to the limitations on how well meteorological models can describe the atmosphere during stable conditions, such as when calm winds prevail. To understand if there are any atmospheric conditions when meteorological models have good performance, for non-afternoon hours, we used atmospheric measurements of carbon dioxide and methane, alongside meteorological model outputs. We found that observations during non-afternoon hours are suitable for use in models when wind speed is greater than 5 m/s. This means that it is possible to double the amount of data that goes into the modeled GHG emission estimates. With this finding, emission estimates will potentially be improved, leading to a better evaluation of the diurnal cycle of GHG emissions.

1 Introduction

To ascertain the fulfilment of the Paris Agreement commitments (United Nations, 2015) and effectively mitigate emissions, we need to quantify emissions at fine scales. Urbanized areas are responsible for about 75 % of CO_2 emissions from global energy use (United Nations Human Settlements Programme, 2022). Several techniques can be used to estimate emissions from cities. Bottom-up approaches use emission factors, direct reporting, and activity data to derive emission

inventories (e.g., Gurney et al., 2012, 2019, 2020; Oda et al., 2018; Keller et al., 2022). Top-down approaches, on the other hand, use atmospheric observations of a trace gas, alongside atmospheric transport models and optimization methods (e.g., Bayesian atmospheric inversion modelling or AIM) to infer emission rates.

AIM is widely used to diagnose emission rates at the global (e.g., Konovalov et al., 2006; McNorton et al., 2022), regional (e.g., Lauvaux et al., 2012; Zhang et al., 2014; Thompson et al., 2015; Alden et al, 2016; Deng et al., 2017; Wang et al., 2020; Barkley et al., 2021; Maasakkers et al., 2021; Petrescu et al., 2021; Deng et al., 2022) and local scale (e.g., Lauvaux et al., 2013, 2016, 2020; Wu et al., 2015; Turner et al., 2020; Nalini et al., 2022). In most cases, AIM assimilates only mid-afternoon observational data (e.g., Lauvaux et al., 2013, 2016; Nalini et al., 2022) since atmospheric transport models have better capability to simulate the convective atmospheric conditions that are common during the afternoon (Mahrt, 1998), as opposed to transient conditions as in the sunrise and sunset hours and the stable atmosphere commonly observed at night. In contrast to continental scale inversions (e.g., Maasakkers et al., 2021) that have substantial sensitivity to all hours of the day despite utilising only mid-afternoon observational data, the shorter transit times of air over the city on the order of few hours mean that city-scale inversions are typically only sensitive to a few hours of the day. This is a limitation to our capability to fully understand diurnal cycles of urban emissions, and affects crucial times of the day when anthropogenic emissions are particularly high (e.g., early morning rush hours).

If an atmospheric transport model makes a small error in simulating the weak mixing typical of a stable boundary layer, the error in mole fraction caused by atmospheric transport can be very large. Stable boundary layers (SBL) mostly occur during nighttime hours and have many underlying physical processes (i.e., sporadic turbulence, internal gravity waves, nocturnal jets, inertial oscillations, drainage flows, land surface coupling and heterogeneity, orographic turbulence) that make them complicated to simulate (Stull, 1988; Steeneveld, 2007, 2014). Similar challenges happen during periods of transition, such as sunrise and sunset hours. As a consequence of the complex interactions among all the physical processes of the SBL, modeled variables such as wind speed and air temperature are often significantly biased (Steeneveld, 2014). On the other hand, convective boundary layers (CBL), which are generally fully developed in the mid-afternoon hours, present buoyancy-generated mixing which homogenizes vertical gradients (VGs; Schmidt & Schumann, 1989; Bakwin et al., 1998; Davis et al., 2003). These physical characteristics make the modelling of the CBL (unstable conditions) more reliable than that of the SBL.

Thus even though tower-based measurements capture the full diurnal cycle of greenhouse gas mole fractions, only a fraction of these data are usually included in AIM. Maier et al. (2022), studied how nighttime observations can be included in AIM for point source emissions estimates using WRF-STILT (Weather Research and Forecasting – Stochastic Time-Inverted Lagrangian Transport model). Using a volume approach for point source emissions, instead of the typical surface emissions approach, they could simulate point source fossil fuel CO_2 during nighttime as well as during the daytime. For urban emissions, Lian et al. (2022) showed an attempt to include morning data in the AIM for emissions estimates during COVID-19 lockdown in Paris. The results showed that fossil fuel estimates, assimilating both morning and afternoon observations, were lower than when exclusively using afternoon observations. This difference was explained as being associated with incorrect BLD simulation at the morning

hours, problems with near-surface vertical mixing, or diurnal cycle of emissions. Thus, using morning data without a filtering criteria was not considered a reliable approach. Then, Lian et al. (2023) used a filtering approach to guide the use of morning and afternoon observations (08:00 - 17:00 UTC) in AIM. The filtering method includes a wind speed threshold used alongside a CO_2, boundary layer depth, and wind direction model-observation mismatch criteria. The inclusion of morning data using this method provided a greater uncertainty reduction in morning hour fossil fuel emission estimates (11 to 16%) when compared to the case of assimilating only afternoon observations. However, there is no attempt to assimilate evening nor night GHG data in urban AIM, especially using a criteria that can be widely used, where certain observations, such as the boundary layer depth, are not available. In the current study, we hypothesize that there are atmospheric conditions during any non-afternoon hours which are relatively well-mixed and thus reliably simulated by atmospheric models, and able to be incorporated into AIM. Our goal is to identify well-mixed atmospheric conditions during non-afternoon hours and test the validity of inclusion of this additional data in AIM. We suggest an approach for filtering observations based on meteorological conditions rather than time of day, enabling more data to be used in AIM, using a simplistic approach that avoids the need for complex additional observations.

To uncover the appropriate atmospheric conditions, we use vertical profiles of trace gases, carbon dioxide (CO_2) and methane (CH_4), from the Indianapolis FLUX Experiment (INFLUX) (Davis et al., 2017) to derive vertical GHG mole fraction differences, normalized by local anthropogenic fossil fuel emissions (Gurney et al., 2012; 2017), as a proxy for atmospheric vertical mixing. Vertical mixing in the afternoon is mainly driven by thermal convection originating from radiative surface heating, which generates thermal turbulence and leads to the development of a well-mixed (unstable) atmospheric layer (Stull, 1988) with well-mixed GHG profiles (Bakwin et al., 1998). The height, from bottom to top, of this mixed layer is herein called boundary layer depth (BLD). During nighttime net radiative cooling at the surface tends to dampen boundary layer turbulence (Stull, 1988). Mechanical turbulence is an important driver of mixing during these hours (Mahrt, 1998; Stull, 1988), thus we examine wind speed to identify turbulent atmospheric conditions.

We partition the vertical differences into surface wind speed categories, as well as into turbulent kinetic energy (TKE) categories. The mean wind speed can characterize the stratification of the stable boundary layer (Mahrt, 1998), and is easily measured. TKE describes the intensity of boundary layer turbulence (Stull, 1988), and although it is not commonly directly measured, it is usually simulated by atmospheric transport models. Nighttime TKE can be high due to the positive buoyancy in urban areas (Tong et al., 2022). This suggests that there might be conditions during non-afternoon hours in urban areas when we will find atmospheric mixing similar to mid-afternoon hours. Thus, we use these measures of turbulence to identify a criteria for the use of additional data in AIM.

Further, we evaluate the transport model performance for the criteria found using this method, to understand whether the well-mixed conditions identified using VGs correspond to the smallest transport model errors. Thus, we investigated the model-observation differences in both wind speed and BLD. We use BLD relative biases to seek the atmospheric conditions that result in the smallest errors. AIM uses trace gas enhancements over background (i.e., CO_2xs) as one of its inputs, comparing observed-modeled enhancements to arrive at the best solution for emissions. Thus, we also explored how observed CO_2xs compares to forward model outputs (Deng et al., 2017), using the Hestia inventory as the prior emissions map (Gurney et al., 2012;

2017), to uncover the atmospheric conditions that lead to the best model-observation agreement. All the results are confronted with typical mid-afternoon conditions, as a reference for acceptable model-observation divergences. Lastly, we discuss how much additional data can be assimilated by AIM through the use of this methodology and how other cities where GHG networks are available can benefit from this method.

2 Methods

2.1 Indianapolis FLUX Experiment (INFLUX) and period of study

We used measurements of CO_2 and CH_4 from the Indianapolis Flux Experiment (INFLUX). The INFLUX observation network is deployed in Indianapolis, Indiana, USA, and is designed to develop and assess methods for greenhouse gas flux measurements and modelling (Davis et al., 2017). This network is equipped with Cavity Ring-Down Spectrometers (CRDS; Picarro, Inc.) and regular discrete flask measurements. As many as 12 telecommunication towers have been instrumented at any one time since 2010 (Miles et al., 2017a; Richardson et al., 2017; Lauvaux et al., 2016), recording high-frequency continuous measurements of CO_2 (all sites), CH_4, and CO (some sites). At some sites, there are measurements at multiple heights. Hourly outputs of these measurements are publicly available (Miles et al., 2017a).

Indianapolis is in predominantly flat terrain, isolated from other metropolitan areas. The city is mostly surrounded by agriculture; and, south of the city, there are forested areas (Figure 1). The prevailing wind directions in Indianapolis are southerly (more frequent during warm months) and westerly (more frequent during cold months), with mean wind speeds at 10 mAGL averaging 3 m/s during the hottest months and 4 m/s during the coldest months. Indianapolis is characterized by a city-scale circulation dominated by advection, where urban emissions are transported downwind the city in plumes, with typical ventilation times of a few hours (e.g., Lauvaux et al., 2016).

For this study, we selected January and February of 2016 to represent the dormant season, and May, June, and July of 2016 to represent the growing season. The dormant season was chosen to evaluate the CO_2 fluxes, which in these months, are less influenced by biological sources (Turnbull et al., 2015; Wu et al., 2022), easing the interpretation of CO_2 analysis. The growing season was used to demonstrate the applicability of the method even when biological CO_2 fluxes are significant. The time period was selected to match other concurrent measurements (e.g., boundary layer depth from Doppler Lidar), explained in Section 2.3.2.

For measurements of CO_2 and CH_4 mole fractions, we selected INFLUX Site 01 and Site 09 (Figure 1) as background sites for the calculation of enhancements (see Section 2.3.3), since they are both considered good upwind backgrounds (Miles et al., 2017b). Site 01 is located at geographical coordinates 39.5805 N and 86.4207 W, and 256 m above sea level (mASL), within a forested area, southwest of the city. Site 09, 39.8627 N and 85.7448 W, 277 mASL, is in an agricultural area and situated east/northeast of the city. From these sites, we used the highest measurement level for the background determination (Section 2.3.3), which are 121 mAGL and 130 mAGL, respectively. We used measurements at 10 m above ground level (mAGL) and 40 mAGL from Site 02 to obtain the vertical differences (Section 2.2) and enhancements (Section 2.3.3). This site is in a suburban area, surrounded by houses and shops and close to a busy interstate highway, on the east side of the city (39.7978 N, 86.0183 W, 267 mASL). We used Halo Photonics Stream Line XR Doppler lidar measurements (Bonin et al., 2018) of boundary layer depth (Section 2.3.2), obtained from a lidar deployed in the northeast corner of Indianapolis

(39.8619 N, 86.0043 W, 21 mAGL; Bonin et al., 2018). Measurements of wind speed (Section 2.3.1) were retrieved from an Automated Surface Observation Station (ASOS, data publicly available at https://mesonet.agron.iastate.edu/) deployed at the Indianapolis International Airport (39.7333 N, 86.2833 W, 10mAGL).

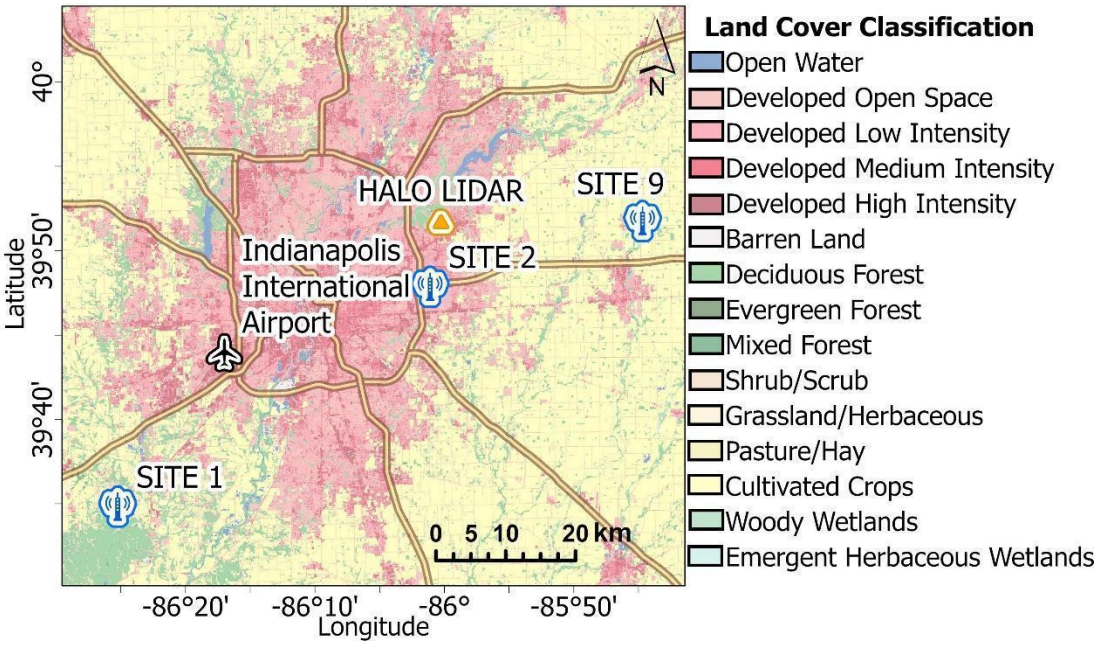

Figure 1. Map with site locations. The tower symbols show the location of INFLUX sites 01, 02, and 09; followed by the Indianapolis International Airport (data publicly available at https://mesonet.agron.iastate.edu/) and the Halo Doppler Lidar (Bonin et al., 2018), used for boundary layer depth analysis (Section 2.3.2). The map background shows the landcover from the 2016 US National Land Cover Database (publicly available at https://www.mrlc.gov/), and the Interstate highways.

We grouped the hours of the day into five periods according to the most likely characteristic of each period (Table 1).

Table 1. Description of the characteristics of each period of the day evaluated. The table highlights the mid-afternoon hours, which are the typical hours used in city-scale AIM. All times are local standard time = UTC - 5 hours.

Local time (LT)	**Name**	**Description**
00:00 – 04:59	Mid-night	Hours when, typically, there is a well-established stable nocturnal boundary layer
05:00 – 08:59	Sunrise/transition	Hours when there is a transition from stable boundary layer to the development of a convective boundary layer
09:00 – 11:59	Morning	Convective boundary layer is developing
12:00 – 16:59	Mid-afternoon	Convective boundary layer is fully developed; typical hours used in AIM
17:00 – 20:59	Sunset/Transition	Transition from convective boundary layer to stable boundary layer
21:00 – 23:59	Evening	Stable boundary layer is developing.

2.2 Proxy for atmospheric vertical mixing

We used vertical gradients (herein defined as VG) of the trace gases (CO_2 and CH_4) to determine if the atmospheric vertical mixing during non-afternoon hours is similar to the vertical

mixing of the same trace gases during mid-afternoon hours. Small vertical differences (where small is defined by the VG observed in mid-afternoon conditions) can be interpreted as well-mixed conditions (unstable CBL). The opposite, large VG relative to mid-afternoon conditions, implies limited vertical mixing, and thus a stable atmospheric surface layer. VGs, however, change with the magnitude of local emission fluxes, which are also variable throughout the day. Thus, for CO_2, we also normalized the VGs by the local, diurnally varying fossil fuel emissions around each tower, obtained from Hestia data product (Gurney et al., 2012; 2017) (details can be found in Text S1). There is one major methane source in Indianapolis, a landfill located in the southwest of the city, and other city wide emissions originate from the natural gas distribution system (Cambaliza et al., 2015). These sources might have seasonal variations, but it is not expected to vary over the diurnal cycle. Thus, it is assumed that CH_4 has a constant flux throughout the day, and a normalization by CH_4 flux is not needed, since the magnitude of the VGs is compared to mid-afternoon hours, cancelling out a constant CH_4 flux.

The averaged VG for a period of time (e.g., 00:00 - 04:59, 05:00 - 08:59, 09:00 - 11:59, 12:00 - 16:59, 17:00 - 20:59, 21:00 - 23:59) of a trace gas mole fraction is calculated by the difference between the top level measurement and the bottom level measurement of the trace gas at each tower, divided by the top-bottom height difference:

$$\overline{VG}[X]_{[time]} = \frac{1}{H}\sum_{hour=1}^{H}\left(\frac{[X(h_1)]_{hour}-[X(h_2)]_{hour}}{h_1-h_2}\right) \quad (1),$$

where $[X(h_1)]_{hour}$ is the trace gas mole fraction (CO_2 or CH_4) at height h_1, and $[X(h_2)]_{hour}$ the trace gas mole fraction at height h_2, both measured at the same hour. Then we averaged the hourly VG from hour 1 to hour H, over each period of time. We computed the vertical differences for Site 02, where h_1 is the measurement at 40 mAGL and h_2 is the measurement at 10 mAGL.

We normalized the $\overline{VG}[X]_{[time]}$ by the averaged vertical gradients during afternoon hours,

$$\widetilde{VG}[X]_{[time]} = \frac{\overline{VG}[X]_{[time]}}{\overline{VG}[X]_{[afternoon]}} \quad (2),$$

and then, for CO_2 we also normalized by averaged fossil fuel emissions ($\overline{ff}_{emissions[time]}$):

$$\widetilde{VG}[CO_2]_{[time;emission]} = \left(\frac{\overline{VG}[CO_2]_{[time]}}{\overline{ff}_{emissions[time]}}\right) / \left(\frac{\overline{VG}[CO_2]_{[afternoon]}}{\overline{ff}_{emissions[afternoon]}}\right) \quad (3).$$

2.3 Determining the tenable atmospheric conditions that lead to inclusion of non-afternoon data

2.3.1 Wind speed and turbulent kinetic energy (TKE)

We used observed wind speed and simulated TKE to determine the tenable conditions for the inclusion of additional data in AIM. After calculating the $\widetilde{VG}[X]_{[time]}$, we subsetted these gradients under different categories of wind speed and TKE to compare to mid-afternoon VGs.

We categorized the $\widetilde{VG}[X]_{[time]}$ for each time period into six wind speed ranges: <2 m/s, 2-3 m/s, 3-4 m/s, 4-5 m/s, 5-6 m/s, > 6 m/s. We used hourly-averaged surface (10 mAGL) wind speed measurements from the Indianapolis International Airport (Figure 1) retrieved from the ASOS network, through the Iowa Environmental Mesonet (publicly available at https://mesonet.agron.iastate.edu/). The choice of publicly available data is helpful to test and expand the method to other cities worldwide.

For TKE we used outputs from 1 km resolution WRF runs for Indianapolis (Deng et al., 2017), extracted at 50 mAGL, providing an alternative criterion that directly represents turbulent mixing and links the observed VGs to the transport model. Similar to wind speed, for each site, we calculated the mean VG within a TKE range, in 0.2 m^2/s^2 intervals, starting from <1.0 m^2/s^2 up to >1.6 m^2/s^2; and then, we normalized by fluxes. We note that TKE is a direct measure of the intensity of atmospheric turbulence, unlike the indirect measure of 10 mAGL wind speed. TKE measurements, however, are not as commonly available, but are computed in many of the boundary layer parameterizations using numerical weather models such as WRF (Weather Research and Forecasting) as a step in AIM.

2.3.2 Model-observation differences

We used hourly-averaged BLD retrieved from a Halo Photonics Stream Line XR Doppler lidar (Bonin et al., 2018; data available online at https://csl.noaa.gov/groups/csl3/measurements/2016influx/halo/), to compare with WRF estimates of BLD (Deng et al., 2017; Deng et al., 2020). Modeled BLD was extracted at the location of the Halo Doppler Lidar (Figure 1). First, we evaluated hourly absolute and fractional biases between model and observation, averaged for each period of the day, to understand if the biases during non-afternoon hours were significantly different from the biases from the mid-afternoon hours. Secondly, we looked at the mean absolute error (MAE) and model-observation bias under the wind speed and TKE classes explained in Section 2.3.1; e.g., calculated the biases for very stable cases and for relatively well-mixed cases during non-afternoon hours. We hypothesized that if the fractional model-observation differences are on the same order of magnitude for both afternoon and non-afternoon hours, then it should be reasonable to extrapolate the use of such observations in AIM.

For surface wind speed, we calculated model-observation correlation and biases to determine the weather model capability to reproduce surface wind speed, seeking good agreement that can justify the use of wind speed as a criterion to determine suitable atmospheric conditions for the use of data in AIM.

2.3.3 Enhancements over a background

We calculated enhancements over background (or X_{xs}) for Site 02 (inlet height 40 mAGL) using an upwind site located outside of the urban plume, thus, either Site 01 (inlet height

121 mAGL) or Site 09 (inlet height 130 mAGL). Site 01 was adopted when air masses were coming from 180 – 360 degrees, and Site 09, otherwise. The measurements were matched in time, thus the X_{xs} at, for example 13:00 LT, represents the difference between the mole fraction at Site 02 at 13:00 LT and the mole fraction measured at Site 01 or 09 at 13:00 LT, following the equation 4:

$$X_{xs} = [X] - [X]_{bg} \quad (4),$$

where $[X]$ is the observed CO_2 mole fraction at Site 02, and the $[X]_{bg}$ is the mole fraction at the background site (e.g., 01 or 09). $[X]$ and $[X]_{bg}$ are measured at the same time.

Modeled X_{xs} can be derived from forward models, through the use of influence functions, also called footprints. An influence function gives us the history information of the airmass that travels to a receptor (a certain place), arriving at a certain time. In our study, the receptor is our site location (e.g., Site 02) where we have a trace gas mole fraction measurements. We used a Lagrangian Particle Dispersion Model (LPDM) and a weather model (WRF) to obtain the influence function at each site (Uliasz et al., 1994; Deng et al., 2017). The model was set up so the influence function results in a gridded map of a trace gas concentration per unit mass per unit time (e.g., ppb/(mol/h)), and it is produced for 72 hours back in time. The domain of the influence function is 87x87 km^2, with 1 km^2 resolution, centered at downtown Indianapolis (39.7597 N, 86.1472 W). To compute X_{xs}, we combined the influence function with the Hestia prior emissions map (Gurney et al., 2012; 2017), which is an emission product based on bottom-up methods, developed for Indianapolis, providing sectorized fossil fuel CO_2 (spatial scale of individual buildings, road segments, and industrial/electricity production facilities) at fine temporal resolution (1 hour). We computed the modeled enhancements of CO_2, $[X]_{xs\_m}$, at a given observation point, i, using:

$$[X]_{xs\_m} = H_i x \quad (5),$$

where H_i is the influence function at a given site i computed using WRF and LPDM, and x is the emission map. Here we assumed that emissions from Hestia (Gurney et al., 2012; 2017) at night are as well known as during the day, and if observation-model differences are the same order of magnitude as in mid-afternoon, we suggest that AIM can be used during these periods with reliability similar to that of the mid-afternoon hours.

To demonstrate whether X_{xs} are dominated by transport errors, we compared observed enhancements to vertical differences of a trace gas ($[X]_{diff} = [X]_{h_1} - [X]_{h_2}$). If X_{xs} are greater or very close to the vertical differences, then the modeled enhancements are not dominated by transport errors.

2.4 Replicability for growing season

During the growing season, the fluxes of CO_2 are more complex. The spring and summer in Indianapolis have intense biological activity (e.g., Turnbull et al., 2015), with agricultural and natural vegetation adding CO_2 fluxes from photosynthesis and respiration to the anthropogenic emissions. The analyses for $\overline{VG}[CO_2]$ can be repeated if the vertical mixing is normalized $\overline{VG}[CO_2]$ by the total fluxes (fossil fuel and biogenic), to remove the strong dependence of the VGs on local fluxes. In the absence of biogenic fluxes, we applied the method to the growing

season (May, June, and July of 2016) using the normalized $\overline{VG}[CO_2]$ only by estimated anthropogenic fossil fuel fluxes (as in equation 2) and the $\overline{VG}[CH_4]$, which is not influenced by biogenic fluxes, to test how wind speed filtering of our observations performs outside the dormant season. Thus, exactly the same method applied for the dormant season. We evaluated whether seasonality of wind speed and boundary layer depth, and the absence of known biogenic fluxes would impact the method and alter the criteria.

3 Results and discussion

3.1 Atmospheric conditions suitable for the use of non-afternoon measurements in atmospheric inversions during the dormant season

$\widetilde{VG}[X]_{[time]}$ categorized according to observed wind speed, showed a clear pattern indicating that the smallest VGs occur during windy conditions (Figure 2 a,b). For wind speeds <3m/s, the $\widetilde{VG}[CO_2]_{[time]}$ is up to 30 times larger than those observed in the mid-afternoon and the $\widetilde{VG}[CH_4]_{[time]}$ up to 100 times larger than the mid-afternoon. As the wind speed increases, the VGs become closer to mid-afternoon mixing conditions. When wind speed is higher than 5 m/s, the vertical mole fraction gradient does not exceed 2.5 times the mid-afternoon gradients, and for specific times of the day (e.g., 09:00 – 11:59 LT), it is even smaller than the mid-afternoon VGs (Figure 2 a). Similar behavior is seen for $\widetilde{VG}[CH_4]_{[time]}$ (Figure 2 b).

Splitting the $\widetilde{VG}[X]_{[time]}$ using simulated turbulent kinetic energy (TKE), however, showed averaged VGs more evenly distributed across different TKE ranges, thus a less prominent pattern than the one observed when using wind speed (Figure 2 c,d). Morning hours (09:00 – 11:59 LT), however, are consistently similar to mid-afternoon for any TKE value, but for other hours of the day, TKE >1.6 m^2/s^2 showed $\widetilde{VG}[CO_2]_{[time]}$ and $\widetilde{VG}[CH_4]_{[time]}$ comparable to mid-afternoon hours (about 2.5 times the averaged VGs of mid-afternoon hours), making this value a recommended cut-off. However, this less prominent pattern observed for TKE versus wind speed suggests that TKE is a less straightforward criterion to determine suitable conditions for inclusion of additional data in AIM. We note that, in urban areas, positive buoyancy may be observed even for nighttime, opposite to what is seen in other landscapes (Tong et al., 2022).

The transport model generally underestimates the observed surface wind speed, but has a strong correlation at all hours of the day during the dormant season. The lowest r^2 (0.80) is found for the period between 05:00 - 08:00 LT, while the highest r^2 (0.90) was found during the late morning hours (09:00 - 11:00 LT) , indicating good model performance for this variable (Figure S1). Thus, wind speed is a straightforward variable to determine the inclusion of additional data in AIM, given that the model and observations have good agreement and showed to be a good proxy for atmospheric stability. For this reason, the following results will be focused on the use of wind speed as the variable to determine a criterion for suitable atmospheric conditions for inclusion of data in AIM.

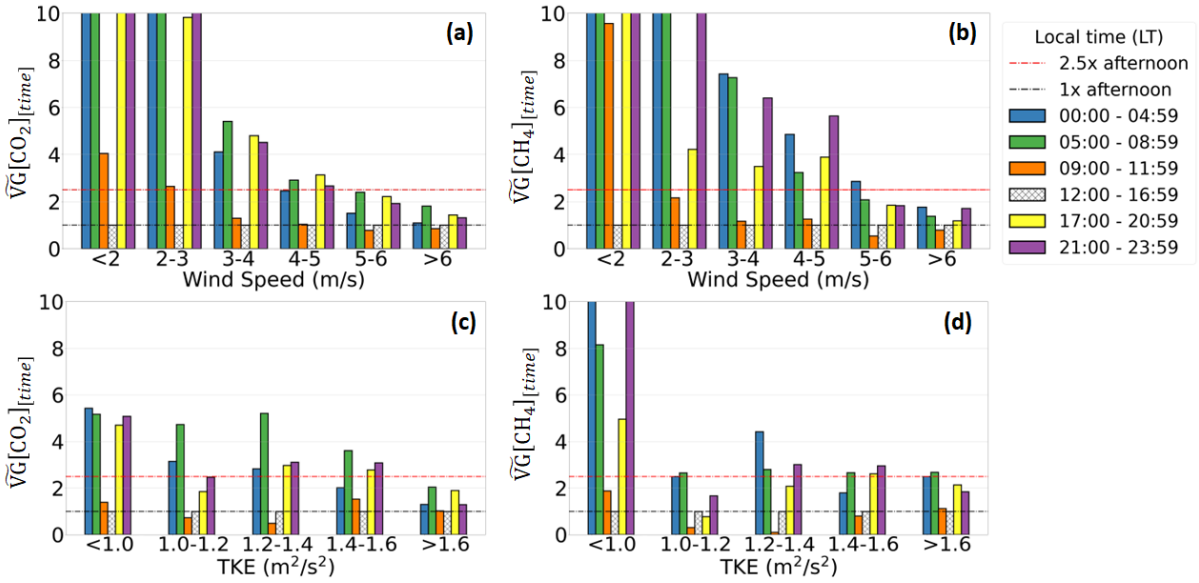

Figure 2. Mean vertical gradients normalized by the mid-afternoon (12:00 to 16:59 local time) vertical gradients ($\widetilde{VG}[X]_{[time]}$) and categorized according to observed wind speed (from Indianapolis International Airport) and modeled turbulent kinetic energy (TKE), for different time periods of the day, for January and February 2016. (a) Wind speed and normalized vertical gradients of CO_2; (b) wind speed and normalized vertical gradients of CH_4; (c) turbulent kinetic energy and normalized vertical gradients of CO_2; (d) turbulent kinetic energy and normalized vertical gradients of CH_4. The black dashed line represents the size of the mid-afternoon VG, while the red dashed line represents 2.5 times the size of the mid-afternoon VG. Figures are limited to 10 times the mid-afternoon VG for better visualization. Note that, in this figure, the vertical gradients of CO_2 are not normalized by fossil fuel emissions (which is done in Figure 3).

A similar pattern was also observed using the absolute VGs for both species, and the smallest gradients occur during the mid-afternoon hours, when the atmosphere is well-mixed, independent of the wind speed (Figure S2). These mid-afternoon VGs typically range from -0.02 to -0.06 ppm/m of CO_2 and from -0.04 up to -0.40 ppb/m of CH_4. For calm winds (<2 m/s), VGs are the largest in magnitude for hours between 00:00 – 08:59 LT and 17:00 – 23:59 LT. This overall pattern is not surprising since mechanical turbulence is a function of wind speed, and increased turbulence will decrease the mole fraction VGs. In the mid-afternoon hours, e.g., 12:00 – 16:59 LT, buoyancy typically produces additional turbulence, and this is reflected in the small magnitude of the VGs at this time. Not coincidentally, these are the typical hours included in atmospheric inversions for GHG emissions estimates. Further, we found that VGs are most sensitive to changes in wind speed for non-afternoon hours, when buoyant mixing is relatively weak.

Even though fluxes vary over the day, the normalization by local fossil fuel flux did not affect the overall pattern observed when using the VGs alone (Figure 3), but revealed similar ratios between $\widetilde{VG}[CO_2]_{[time;emission]}$ across all hours the day (Figure S3). This indicates that VGs are not highly sensitive to atmospheric transport errors for windy conditions. We noted that only minor differences were found when compared to mid-afternoon conditions. Thus, for the dormant season, the VGs did not show strong sensitivity to the fossil fuel flux diurnal cycle, allowing for a simplified interpretation of VGs.

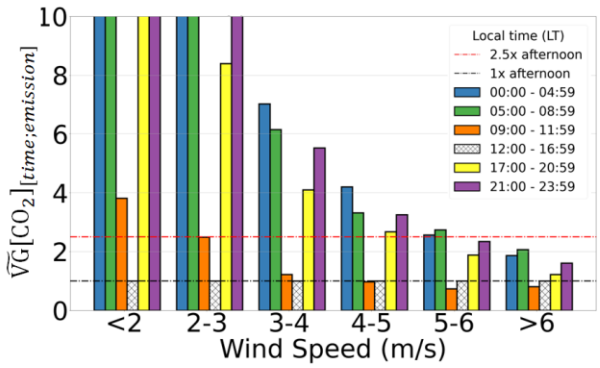

Figure 3. Mean vertical gradients normalized by fossil fuel emissions (details can be found in Text S1) and by the normalized mid-afternoon (12:00 to 16:59 LT) vertical gradient (equation 2) and categorized according to observed wind speed (from Indianapolis International Airport) for different time periods of the day, for January and February of 2016.

Using a trace gas assumed to have small or no diurnal variation in emissions, such as CH_4, enables us to examine if the results for CO_2 are driven primarily by changes in turbulence or fluxes. The similarity in results for both CO_2 and CH_4 during the dormant season suggests that these results are representative primarily of changes in mixing. Thus, it indicates one can use the method for either tracer gas interchangeably, and extend this methodology into the growing season, when biogenic fluxes can be a confounding factor (see Section 3.4).
We also noted that using modeled wind speed to categorize VGs resulted in the same overall pattern as using observed wind speed (Figure S4). However, since the model underestimates surface wind speed, one possible caveat, is that using the modeled wind speed can reduce the amount of data that could possibly be included, since less observations will match the criterion (e.g., fewer observations when modeled wind speed is greater than 5 m/s).

3.2 Boundary layer depth assessment for different criteria

For January and February of 2016, on average, the WRF model underestimates BLD during the mid-afternoon hours regardless the wind speed during the dormant season, while for non-afternoon hours, when wind speed is lower than 3 m/s, the opposite is observed (Figure S5 a). It suggests that, under light wind conditions, the modeled buoyancy flux might be overestimated, resulting in an excessive growth of the BLD during non-afternoon hours (Figure S6).

For non-afternoon hours, the relative model-observation mismatch in boundary layer depth decreased as wind speed increased, and for wind speed greater than 5 m/s, the absolute relative bias decrease to less than ~(±)30% (Figure 4). When wind speed is lower than 5 m/s, averaged bias typically exceed 100%. For mid-afternoon, averaged biases did not exceed -21%, with the only exception at calm winds (<2 m/s), indicating that this period of the day satisfactorily reproduces the BLD.

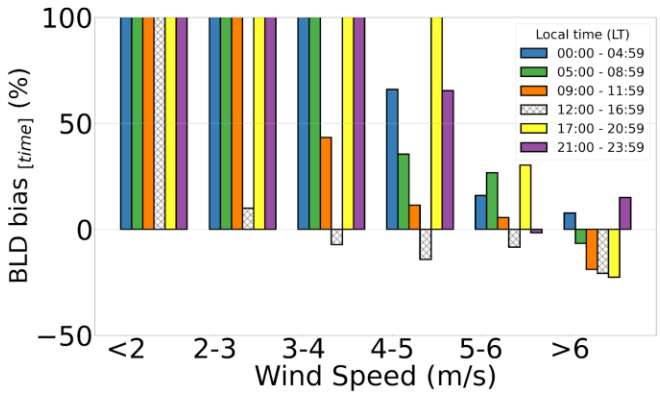

Figure 4. Mean boundary layer depth (BLD) bias (mean mismatch between hourly modeled and observed BLD) for different time ranges shown at local time (LT), categorized by wind speed classes, for January and February 2016.

It is important to note that the presented biases are averaged over the selected periods of time, and there might be many hours when the mismatches will exceed 30%. We, then, looked at the number of non-afternoon hours that will meet both conditions, i.e., relative BLD bias smaller than 30% at wind speed greater than 5 m/s. We found that 65% of the hours will have both conditions.

Thus, during the dormant season, we found that when wind speed is above 5 m/s, VGs are about 2.5 times the typical mid-afternoon VGs, and the BLD bias is also smallest (30%) under these conditions. We found that both conditions are met for the majority of the non-afternoon hours. Given the similarity of these conditions to typical mid-afternoon hours, we concluded that GHG mole fractions, when wind speed is greater than 5 m/s, for any hour of the day, can be used in AIM for Indianapolis.

3.3 CO_2xs during the dormant season

Modeled CO_2xs overestimate the observations for all hours of the day (Figure 5 a,b). The averaged CO_2xs normalized by fossil fuel emissions and boundary layer depth, either observed and modeled, have similar magnitude across all hours of the day for windy conditions (Figure 5 c,d). This shows that under low wind speeds, CO_2xs are much more subjected to transport errors.

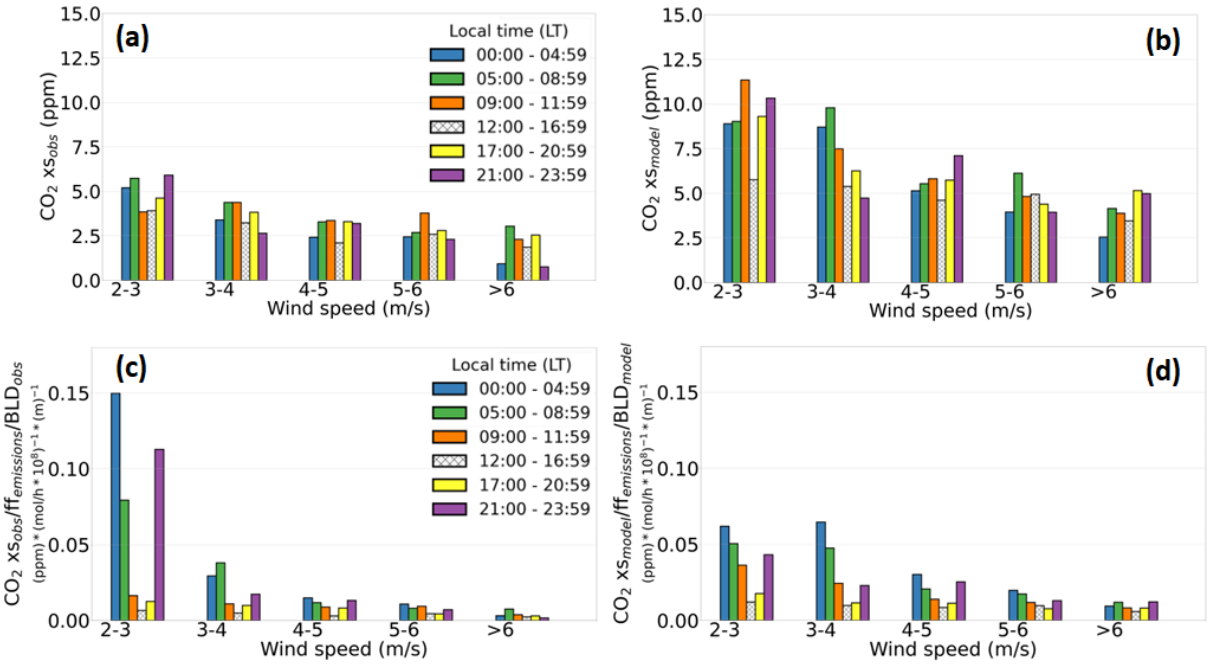

Figure 5. Mean CO_2 enhancement for January and February 2016. (a) Observed enhancements (CO_2xs obs). (b) Modeled enhancements (CO_2xs model). (c) Observed enhancement normalized by fossil fuel emissions and observed boundary layer depth. (d) Modeled enhancements normalized by fossil fuel emissions and modeled boundary layer depth.

We also note that since no filtering of atmospheric conditions is needed to use the data for mid-afternoon hours (i.e., atmospheric transport is well simulated, reproducing consistent CO_2xs for all wind conditions), it is justifiable that previous work has only included mid-afternoon hours. There is little change in MAE and bias during the afternoon with wind speed (Table 2). This is opposite to the remaining hours of the day, when MAE and bias dramatically decrease with more turbulent conditions. The model-observation performance also diverges significantly for non-afternoon hours due to problems in the modeled atmospheric transport, as also seen by the BLD model-observations performance.

Table 2. CO_2 enhancement mean, mean absolute error (MAE), and bias from all conditions, for atmospheric conditions when wind speed is smaller than 5 m/s, and greater than or equal to 5 m/s. All times are in local time = UTC-5. * The mean refers to the observed CO_2 enhancement.

Local time (LT)	**CO_2xs (all conditions)**			**CO_2xs (wind speed <5 m/s)**			**CO_2xs (wind speed ≥5 m/s)**		
	MEAN* (ppm)	MAE (ppm)	BIAS (ppm)	MEAN* (ppm)	MAE (ppm)	BIAS (ppm)	MEAN* (ppm)	MAE (ppm)	BIAS (ppm)
00:00-04:59	2.6	4.4	3.1	3.3	5.6	4.5	1.6	2.7	1.5
05:00-08:59	3.8	4.3	3.4	4.3	4.9	4.0	2.9	3.1	2.3
09:00-11:59	3.1	3.3	2.5	3.8	4.6	3.5	2.7	2.4	1.7
12:00-16:59	2.2	2.4	1.9	2.7	2.9	2.2	2.0	2.2	1.8
05:00-20:59	3.2	3.9	2.6	3.8	4.4	2.9	2.6	3.3	2.3
09:00-23:59	2.5	4.8	3.4	3.8	5.7	3.7	1.2	3.8	3.1

We also observed that CO_2xs is typically larger than vertical differences for all hours of the day with >5 m/s wind speed, and similar to mid-afternoon conditions, showing that the trace gas signal is not dominated by VGs (Figure 6 b). Yet for calmer wind conditions, we noticed the

enhancements are more susceptible to transport errors, shown by averaged vertical differences that can be greater than the enhancements, mainly noted between 05:00 - 08:50 LT and 21:00 - 23:59 LT (Figure 6 a). Thus, in stable atmospheric conditions, simulation of VGs is more sensitive to transport errors.

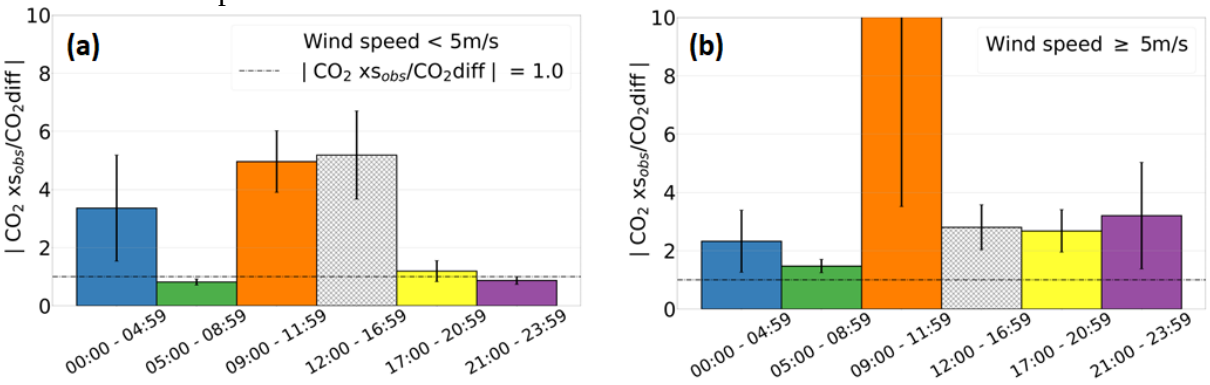

Figure 6. Absolute mean of hourly observed CO_2 enhancement (Site 02 - background) normalized by CO_2 vertical differences (Site 02) for January and February of 2016. (a) Wind speed < 5 m/s. (b) Wind speed ≥ 5 m/s. In (b) the scale is cut-off at 10; the morning (09:00-11:59 LT) averaged ratio between CO_2xs_{obs} and CO_2diff is ~17. Note that this large difference might be due to rapid changes in VGs during these hours of the day. Error bars are the standard error of the mean. Hours are in local time. Using Site 02 inlet height 40 mAGL, background is either Site 01 (inlet height 121 mAGL) or Site 09 (inlet height 130 mAGL). Site 01 was adopted when air masses were coming from 180 – 360 degrees, and Site 09, otherwise.

3.4 Growing season

Growing season $\widetilde{VG}[CO_2]_{[time]}$ and $\widetilde{VG}[CH_4]_{[time]}$ (Figure S7), and $\widetilde{VG}[CO_2]_{[time;emission]}$ (Figure S8), showed similar patterns as in the dormant season, with VGs becoming closer to zero with the increased wind speed. We assume that the large differences in VGs during the morning hours might be related to rapid changes in VGs that occur about this time of day (09:00 - 11:59 LT), due to the rapid changes in surface warming that occur within these warm months (May through July).

There is seasonality in the wind speed, with the growing season being characterized by calmer winds than the dormant season. WRF simulated calm winds less robustly, resulting in smaller model-observation correlation for all hours of the day, when compared to the dormant season, although still underestimating the observations (Figure S9). The smallest correlation between these variables (r^2 = 0.40) is found at late hours of the day (21:00 - 23:59 LT), while the strongest correlations were found at late morning (09:00 - 11:59 LT), r^2 = 0.80, and mid-afternoon (12:00 - 16:59 LT), r^2 = 0.76. The mean bias is also significantly larger for wind speed greater than 5 m/s (Figure S10) than during the dormant season (Figure S6), for non-afternoon hours, possibly due to fewer observations within this wind range. Biases for these hours varied from -1.7 m/s (09:00 - 11:59 LT) to -2.8 m/s (21:00 - 23:59 LT). For mid-afternoon hours, the bias for unstable conditions (-1.5 m/s) is only slightly greater than the observed during the dormant season (-1.3 m/s). This discrepancy can be explained by the reduced frequency of strong wind speeds during non-afternoon hours compared to the dormant season. A direct consequence of using the wind speed as a criterion is that we expect that fewer observations during the growing season will be included in the AIM, which can possibly create noise, due to fewer observations, in posterior emissions estimates for non-afternoon hours.

The boundary layer also has seasonality, and similar to wind speed, we found larger biases for the growing season than for the dormant season. The smallest mean relative bias that encompasses all hours of the day is 40% (opposed to 31% for dormant season), when wind speed is greater than 6 m/s (opposed to 5 m/s during the dormant season) (Figure S11). This relative bias corresponds to non-afternoon VGs up to 5.5 times larger than typical afternoon VGs, when wind speed is greater than 6 m/s (Figure S12). For wind speeds greater than 5 m/s, we found that in the late hours of the day (21:00 - 23:59 LT), the BLD bias exceeded 100%, but for all the remaining hours, it is kept below 40%. For these wind conditions (except for 21:00 - 23:59 LT), we also found that VGs are less than 5.5 times the typical afternoon $\overline{VG}[CO_2]$. $\overline{VG}[CH_4]$ were so small in the mid-afternoon (close to zero), that non-afternoon conditions easily exceeded 10 times the afternoon VGs (Figure S12). Thus, although we initially assumed that CH_4 would be an alternative to avoid the complications of the CO_2 biogenic fluxes, both trace gases showed similar patterns that can indicate the most likely atmospheric conditions for data usage. Looking at the CO_2xs normalized by local anthropogenic fossil fuel emissions and boundary layer depth (Figure S13), we note that, as in the dormant season, there is a more consistent behavior of the normalized CO_2xs as the wind becomes strong, for both observed and modeled variables. Large discrepancies were observed for early and late hours of the day. Unlike the VGs,it may be necessary to normalize the growing season CO_2xs by biogenic as well as fossil fuel fluxes. Hence, the large discrepancies might be associated with biogenic respiration not accounted for in this study.

Lastly, replicating the ratio between observed CO_2xs and the vertical differences, we note that, on average, for the growing season, the CO_2xs are typically larger than the vertical differences for all wind speed conditions (Figure S14). The only exception is when wind is greater than 5 m/s at late hours of the day. This is consistent with the large BLD and wind speed biases found within these hours, which is likely due to the small amount of data available in this category. Another important caveat for this specific analysis is that biological fluxes might be largely impacting the background sites during the growing season, making these enhancements (without accounting for biogenic fluxes) not be a good representation of anthropogenic emissions.

Thus, despite of the seasonality of the variables (e.g., CO_2 fluxes, wind speed, boundary layer depth), combining all the results, there is not a significant difference between the patterns observed for dormant and growing season, indicating that 5 m/s is a reasonable criterion for both seasons.

3.5 Expected non-afternoon observations to be added in urban AIM

Using only mid-afternoon hours and excluding calm winds (e.g., <2 m/s), 21% of the data is retained for Indianapolis. Retaining only the non-afternoon hours for which the wind speed is ≥5 m/s results in adding an additional 37% of the data for a total of 58% of the available data, close to tripling the amount of data used (Figure 7).

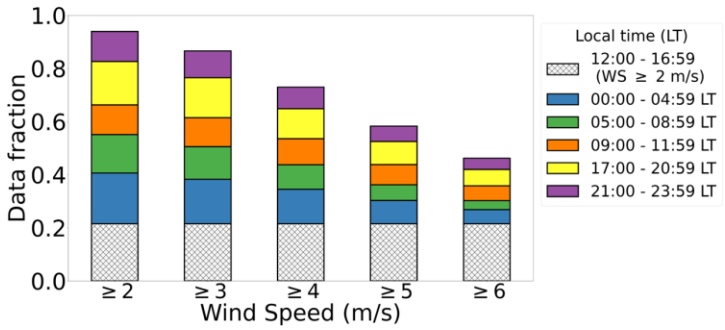

Figure 7. Data fraction from the total 24 hours of measurements by period of time using wind speed criteria. Baseline is mid-afternoon hours (12:00 – 16:59 LT) for all wind conditions (excluding calm wind).

Using the same wind speed criteria derived for Indianapolis, we examined the fraction of data that could be retained for other cities around the world which already have GHG observational networks (Figure 8), using wind speed data from the closest international airport of these cities (ASOS network), through the Iowa Environmental Mesonet (publicly available at https://mesonet.agron.iastate.edu/), for the year of 2021. We note each city has its own meteorological characteristics. For example, Melbourne has strong winds during night-time, while in Los Angeles, the wind is the strongest in the sunset transition hours. Since turbulent mixing near the surface is tightly connected to near-surface winds, we can extrapolate our findings to other cities using the wind conditions for these cities.

The wind speed criterion derived from Indianapolis gives an indication of the additional data that could be added for other cities. Windier cities like Melbourne, Auckland, and Boston benefit strongly, since there are a large number of hours that fall within wind speeds higher than 5 m/s. Cities with calmer winds like Zurich and Sao Paulo would add far less additional data. We do, however, recommend that before including additional data into AIM for other cities, a more rigorous analysis such as presented here for Indianapolis should be performed, as we have insufficient evidence to determine that 5 m/s is an appropriate wind speed threshold for all cities.

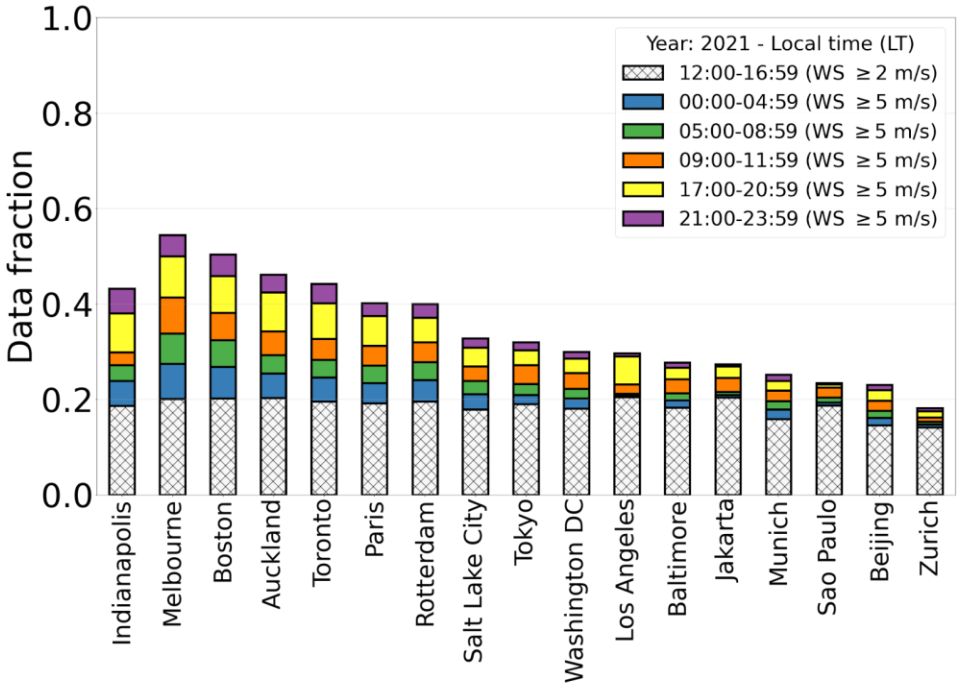

Figure 8. Data fraction that will be added into inversion models for different cities when wind speed is ≥ 5m/s, on top of the data fraction typically used on inverse systems (mid-afternoon) when removing calm winds (≤ 2m/s). This is based on 2021 wind speed datasets from the international airports as a representation of wind conditions in the cities where there is a greenhouse gas network in place. Indianapolis is used as a reference, and the other cities are sorted by largest to smallest data fraction.

4 Conclusions

We have identified a simple wind speed criterion that can be used to add GHG enhancement observations to AIMs outside of the afternoon conditions typically used for AIMs. Analysis of vertical gradients of CO_2 and CH_4 categorized by different wind speed conditions indicated the most likely atmospheric conditions that can lead to the use of additional data in AIM. Further analysis that linked the model performance to the observed vertical gradients, confirmed that under unstable conditions, biases in BLD and enhancements are much smaller than under atmospheric stable conditions.

The use of additional data under relatively well-mixed atmospheric conditions will allow us to begin to use urban AIMs to study critical hours of the day, when emissions are at their highest levels in specific sectors. One example are the traffic rush hours, which fall within the transition of atmospheric conditions, close to sunset and sunrise hours, which means abrupt changes in the atmospheric boundary layer depth. Our analyses suggest that by selecting relatively windy atmospheric conditions, e.g., ≥ 5 m/s, data throughout the day can be applied to AIMs without introducing inordinately large errors in atmospheric transport. This criterion will allow to more than double the amount of data available to be assimilated by AIMs, which in urban environments will allow AIMs to better estimate fluxes for all hours of the day.

Acknowledgments

This work was supported by CarbonWatch-NZ MBIE Endeavour Research Programme (C01X1817) and the US National Institute of Standards and Technology's urban GHG testbeds program (Award #: 70NANB19H128). The first author is funded by the Wellington Doctoral Scholarship at Victoria University of Wellington.

Open Research

Trace gas mole fractions observations (Miles et al., 2017a) are available online at The Pennsylvania State University Data Commons, https://doi.org/10.18113/D37G6P.

Doppler lidar observations (Bonin et al., 2018) are available online at https://csl.noaa.gov/groups/csl3/measurements/2016influx/halo/.

Hestia product (Gurney et al., 2012) is available online at https://hestia.rc.nau.edu/Data.html.

Weather model outputs (Deng et al., 2020) are available online at The Pennsylvania State University Data Commons, https://doi.org/10.26208/z04g-3h91.

ASOS (Automated Surface Observation Station) observations are available online through the Iowa Environmental Mesonet (https://mesonet.agron.iastate.edu/).

2016 US National Land Cover Database (used for Figure 1) is available online through the Multi-Resolution Land Characteristics (MRLC) Consortium (https://www.mrlc.gov/).

References

Alden, C. B., Miller, J. B., Gatti, L.V., Gloor, M. M., Guan, K., Michalak, A. M., et al. (2016). Regional atmospheric CO_2 inversion reveals seasonal and geographic differences in Amazon net biome exchange. *Global change biology*, 22(10), 3427-3443. https://doi.org/10.1111/gcb.13305

Bakwin, P. S., Tans, P. P., Hurst, D. F., & Zhao, C. (1998). Measurements of carbon dioxide on very tall towers: results of the NOAA/CMDL program. *Tellus B: Chemical and Physical Meteorology*, 50(5), 401-415. https://doi.org/10.3402/tellusb.v50i5.16216

Barkley, Z. R., Davis, K. J., Feng, S., Cui, Y. Y., Fried, A., Weibring, P., et al. (2021). Analysis of oil and gas ethane and methane emissions in the southcentral and eastern United States using four seasons of continuous aircraft ethane measurements. *Journal of Geophysical Research: Atmospheres*, 126, e2020JD034194, 1-17. https://doi.org/10.1029/2020JD034194

Bonin, T. A., Carroll, B. J., Hardesty, R. M., Brewer, W. A., Hajny, K., Salmon, O. E., & Shepson, P. B. (2018). Doppler lidar observations of the mixing height in Indianapolis using an automated composite fuzzy logic approach. *Journal of Atmospheric and Oceanic Technology*, 35(3), 473–490. https://doi.org/10.1175/JTECH-D-17-0159.1

Cambaliza, M. O. L., Shepson, P. B., Bogner, J., Caulton, D. R., Stirm, B., Sweeney, C., et al. (2015). Quantification and source apportionment of the methane emission flux from the city of Indianapolis. *Elementa: Science of the Anthropocene*, 3:000037, 1-18. https://doi.org/10.12952/journal.elementa.000037

Davis, K. J., Bakwin, P. S., Yi, C., Berger, B. W., Zhao, C., Teclaw, R. M., & Isebrands, J. G. (2003). The annual cycles of CO_2 and H_2O exchange over a northern mixed forest as observed

from a very tall tower. *Global Change Biology*, 9(9), 1278-1293. https://doi.org/10.1046/j.1365-2486.2003.00672.x

Davis, K. J., Deng, A., Lauvaux, T., Miles, N. L., Richardson, S. J., Sarmiento, D. P., et al. (2017). The Indianapolis Flux Experiment (INFLUX): A test-bed for developing urban greenhouse gas emission measurements. *Elementa: Science of the Anthropocene*, 5:21, 1-20. https://doi.org/10.1525/elementa.188

Deng, A., Lauvaux, T., Davis, K. J., Gaudet, B. J., Miles, N., Richardson, S. J., et al. (2017). Toward reduced transport errors in a high resolution urban CO_2 inversion system. *Elementa: Science of the Anthropocene*, 5:20, 1-20. https://doi.org/10.1525/elementa.133

Deng, A., Lauvaux, T., Miles, N., Davis, K. J., & Barkley, Z. R. (2020). Meteorological fields over Indianapolis, IN from the Weather Research and Forecasting model (WRF v3.5.1) [Dataset]. The Pennsylvania State University Data Commons. https://doi.org/10.26208/z04g-3h91

Deng, Z., Ciais, P., Tzompa-Sosa, Z. A., Saunois, M., Qiu, C., Tan, C., et al. (2022). Comparing national greenhouse gas budgets reported in UNFCCC inventories against atmospheric inversions. *Earth System Science Data*, 14(4), 1639–1675. https://doi.org/10.5194/essd-14-1639-2022

Gurney, K. R., Razlivanov, I., Song, Y., Zhou, Y., Benes, B., & Abdul-Massih, M. (2012). Quantification of fossil fuel CO_2 emissions on the building/street scale for a large U.S. City. *Environmental Science and Technology*, 46(21), 12194–12202. https://doi.org/10.1021/es3011282

Gurney, K. R., Liang, J., Patarasuk, R., O'Keeffe, D., Huang, J., Hutchins, M., et al. (2017). Reconciling the differences between a bottom-up and inverse-estimated $FFCO_2$ emissions estimate in a large US urban area. *Elementa: Science of the Anthropocene*, 5: 44, 1-12. https://doi.org/10.1525/elementa.137

Gurney, K. R., Patarasuk, R., Liang, J., Song, Y., O'keeffe, D., Rao, P., et al. (2019). The Hestia fossil fuel CO_2 emissions data product for the Los Angeles megacity (Hestia-LA). *Earth System Science Data*, 11(3), 1309–1335. https://doi.org/10.5194/essd-11-1309-2019

Gurney, K. R., Liang, J., Patarasuk, R., Song, Y., Huang, J., & Roest, G. (2020). The Vulcan Version 3.0 High-Resolution Fossil Fuel CO_2 Emissions for the United States. *Journal of Geophysical Research: Atmospheres*, 125(19), 1–27. https://doi.org/10.1029/2020JD032974

Keller, E. D., Hilton, T. W., Benson, A., Karalliyadda, S., Xie, S., Gurney, R., & Turnbull, J. C. (2021). Mahuika-Auckland : A spatially and temporally resolved fossil fuel CO_2 emissions data product for Auckland, New Zealand. *Geoscience Data Journal*, 10(3), 347-367. https://doi.org/10.1002/gdj3.181

693 Konovalov, I. B., Beekmann, M., Richter, A., & Burrows, J. P. (2006). Inverse modelling of the
694 spatial distribution of NOx emissions on a continental scale using satellite data. *Atmospheric*
695 *Chemistry and Physics*, 6(7), 1747-1770. https://doi.org/10.5194/acp-6-1747-2006
696
697 Lauvaux, T., Schuh, A. E., Uliasz, M., Richardson, S., Miles, N., Andrews, A. E., et al. (2012).
698 Constraining the CO_2 budget of the corn belt: exploring uncertainties from the assumptions in a
699 mesoscale inverse system. *Atmospheric Chemistry and Physics*, 12(1), 337-354.
700 https://doi.org/10.5194/acp-12-337-2012
701
702 Lauvaux, T., Miles, N. L., Richardson, S. J., Deng, A., Stauffer, D. R., Davis, K. J., et al. (2013).
703 Urban emissions of CO_2 from Davos, Switzerland: The first real-time monitoring system using
704 an atmospheric inversion technique. *Journal of Applied Meteorology and Climatology*, 52(12),
705 2654–2668. https://doi.org/10.1175/JAMC-D-13-038.1
706
707 Lauvaux, T., Miles, N. L., Deng, A., Richardson, S. J., Cambaliza, M. O., Davis, K. J., et al.
708 (2016a). High-resolution atmospheric inversion of urban CO_2 emissions during the dormant
709 season of the Indianapolis flux experiment (INFLUX). *Journal of Geophysical Research*,
710 121(10), 5213–5236. https://doi.org/10.1002/2015JD024473
711
712 Lauvaux, T., Gurney, K.R., Miles, N.L., Davis, K.J., Richardson, S.J., Deng, A., et al. (2020).
713 Policy-relevant assessment of urban greenhouse gas emissions. *Environmental Science &*
714 *Technology*, 54(16), 10237-10245. https://doi.org/10.1021/acs.est.0c00343
715

716 Lian, J., Lauvaux, T., Utard, H., Bréon, F. M., Broquet, G., Ramonet, M., et al. (2022).
717 Assessing the effectiveness of an urban CO_2 monitoring network over the Paris region through
718 the COVID-19 lockdown natural experiment. *Environmental Science & Technology*, 56(4),
719 2153-2162. https://doi.org/10.1021/acs.est.1c04973
720
721 Lian, J., Lauvaux, T., Utard, H., Bréon, F.M., Broquet, G., Ramonet, M., et al. (2023). Can we
722 use atmospheric CO_2 measurements to verify emission trends reported by cities? Lessons from a
723 6-year atmospheric inversion over Paris. *Atmospheric Chemistry and Physics*, 23(15), 8823-
724 8835. https://doi.org/10.5194/acp-23-8823-2023
725
726 Maasakkers, J. D., Jacob, D. J., Sulprizio, M. P., Scarpelli, T. R., Nesser, H., Sheng, J., et al.
727 (2021). 2010-2015 North American methane emissions, sectoral contributions, and trends: A
728 high-resolution inversion of GOSAT observations of atmospheric methane. *Atmospheric*
729 *Chemistry and Physics*, 21(6), 4339–4356. https://doi.org/10.5194/acp-21-4339-2021
730
731 Mahrt, L. (1998). Stratified atmospheric boundary layers and breakdown of models. *Theoretical*
732 *and Computational Fluid Dynamics*, 11, 263–279. https://doi.org/10.1007/s001620050093
733
734 Maier, F., Gerbig, C., Levin, I., Super, I., Marshall, J., & Hammer, S. (2022). Effects of point
735 source emission heights in WRF–STILT: a step towards exploiting nocturnal observations in
736 models. *Geoscientific Model Development*, 15(13), 5391-5406. https://doi.org/10.5194/gmd-15-
737 5391-2022
738

McNorton, J., Bousserez, N., Agustí-Panareda, A., Balsamo, G., Cantarello, L., Engelen, R., et al. (2022). Quantification of methane emissions from hotspots and during COVID-19 using a global atmospheric inversion. *Atmospheric Chemistry and Physics*, 22(9), 5961-5981. https://doi.org/10.5194/acp-22-5961-2022

Miles, N. L., Richardson, S. J., Davis, K. J., & Haupt, B. J. (2017a). In-situ tower atmospheric measurements of carbon dioxide, methane and carbon monoxide mole fraction for the Indianapolis Flux (INFLUX) project, Indianapolis, IN, USA [Dataset]. The Pennsylvania State University Data Commons. https://doi.org/10.18113/D37G6P

Miles, N. L., Richardson, S. J., Lauvaux, T., Davis, K. J., Balashov, N. V., Deng, A., et al. (2017b). Quantification of urban atmospheric boundary layer greenhouse gas dry mole fraction enhancements in the dormant season: Results from the Indianapolis Flux Experiment (INFLUX). *Elementa: Science of the Anthropocene*, 5:27, 1-22. https://doi.org/10.1525/elementa.127

Nalini, K., Lauvaux, T., Abdallah, C., Lian, J., Ciais, P., Utard, H., Laurent, O., & Ramonet, M. (2022). High-resolution Lagrangian inverse modeling of CO_2 emissions over the Paris region during the first 2020 lockdown period. *Journal of Geophysical Research: Atmospheres*, 127(14), 1-26. https://doi.org/10.1029/2021JD036032

Oda, T., Maksyutov, S., & Andres, R. J. (2018). The Open-source Data Inventory for Anthropogenic CO_2, version 2016 (ODIAC2016): a global monthly fossil fuel CO_2 gridded

emissions data product for tracer transport simulations and surface flux inversions. *Earth System Science Data*, 10(1), 87–107. https://doi.org/10.5194/essd-10-87-2018

Petrescu, A.M.R., Qiu, C., Ciais, P., Thompson, R.L., Peylin, P., McGrath, M.J., et al. (2021). The consolidated European synthesis of CH_4 and N_2O emissions for the European Union and United Kingdom: 1990–2017. *Earth system science data*, 13(5), 2307-2362. https://doi.org/10.5194/essd-13-2307-2021

Richardson, S. J., Miles, N. L., Davis, K. J., Lauvaux, T., Martins, D. K., Turnbull, J. C., et al. (2017). Tower measurement network of in-situ CO_2 , CH_4 , and CO in support of the Indianapolis FLUX (INFLUX) Experiment. *Elementa: Science of the Anthropocene*, 5:59, 1-14. https://doi.org/10.1525/elementa.140

Schmidt, H., & Schumann, U. (1989). Coherent structure of the convective boundary layer derived from large-eddy simulations. *Journal of Fluid Mechanics*, 200, 511-562. https://doi.org/10.1017/S0022112089000753

Steeneveld, G. J. (2007). *Understanding and prediction of stable atmospheric boundary layers over land* (Doctoral dissertation). Retrieved from Wageningen University & Research eDepot. (https://edepot.wur.nl/22125). Wageningen University.

782 Steeneveld, G. J. (2014). Current challenges in understanding and forecasting stable boundary
783 layers over land and ice. *Frontiers in Environmental Science*, 2:41, 1-6.
784 https://doi.org/10.3389/fenvs.2014.00041
785
786 Stull, R. (1988). *An introduction to boundary layer meteorology*, Springer Dordrecht.
787 https://doi.org/10.1007/978-94-009-3027-8
788
789 Thompson, R.L., Stohl, A., Zhou, L.X., Dlugokencky, E., Fukuyama, Y., Tohjima, Y., et al.
790 (2015). Methane emissions in East Asia for 2000–2011 estimated using an atmospheric Bayesian
791 inversion. *Journal of Geophysical Research: Atmospheres*, 120(9), 4352-4369.
792 https://doi.org/10.1002/2014JD022394
793
794 Tong, B., Guo, J., Wang, Y., Li, J., Yun, Y., Solanki, R., et al. (2022). The near-surface turbulent
795 kinetic energy characteristics under the different convection regimes at four towers with
796 contrasting underlying surfaces. *Atmospheric Research*, 270, 1-12.
797 https://doi.org/10.1016/j.atmosres.2022.106073
798
799 Turnbull, J. C., Sweeney, C., Karion, A., Newberger, T., Lehman, S. J., Tans, P. P., et al. (2015).
800 Toward quantification and source sector identification of fossil fuel CO_2 emissions from an
801 urban area: Results from the INFLUX experiment. *Journal of Geophysical Research:*
802 *Atmospheres*, 120(1), 292–312. https://doi.org/10.1002/2014JD022555
803

Turner, A. J., Kim, J., Fitzmaurice, H., Newman, C., Worthington, K., Chan, K., et al. (2020). Observed impacts of COVID-19 on urban CO_2 emissions. *Geophysical Research Letters*, 47(22), 1–10. https://doi.org/10.1029/2020GL090037

Uliasz, M., Bartochowska, M., Madany, A., Piwkowski, H., Parfiniewicz, J., & Rozkrut, M. (1994). Application of the mesoscale dispersion modeling system to investigation of air Pollution transport in Southern Poland. In Gryning, SE., Millán, M.M. (Eds.), *Air Pollution Modeling and Its Application X. NATO, Challenges of Modern Society* (Vol. 18, pp. 27-34). Springer, Boston, MA. https://doi.org/10.1007/978-1-4615-1817-4_4

United Nations. (2015). *Paris Agreement*. https://unfccc.int/process-and-meetings/the-paris-agreement. Last accessed on: 01 February 2024.

United Nations Human Settlements Programme. (2022). *Climate Change*. Https://Unhabitat.Org/Topic/Climate-Change. Last accessed on: 01 February 2024.

Wang, J., Feng, L., Palmer, P.I., Liu, Y., Fang, S., Bösch, H., et al. (2020). Large Chinese land carbon sink estimated from atmospheric carbon dioxide data. *Nature*, 586(7831), 720-723. https://doi.org/10.1038/s41586-020-2849-9

Wu, L., Broquet, G., Ciais, P., Bellassen, V., Vogel, F., Chevallier, F., Xueref-Remy, I., & Wang, Y. (2015). Atmospheric inversion for cost effective quantification of city CO_2 emissions.

826 *Atmospheric Chemistry & Physics Discussions*, 15(21), 30693–30756.
827 https://doi.org/10.5194/acpd-15-30693-2015
828
829 Wu, K., Davis, K. J., Miles, N. L., Richardson, S. J., Lauvaux, T., Sarmiento, D. P., et al. (2022).
830 Source decomposition of eddy-covariance CO_2 flux measurements for evaluating a high-
831 resolution urban CO_2 emissions inventory. *Environmental Research Letters*, 17(7), 074035, 1-10.
832 https://doi.org/10.1088/1748-9326/ac7c29
833
834 Zhang, H., Chen, B. Z., van der Laan-Luijkx, I. T., Chen, J., Xu, G., Yan, J. W., et al. (2014).
835 Net terrestrial CO_2 exchange over China during 2001–2010 estimated with an ensemble data
836 assimilation system for atmospheric CO_2. *Journal of Geophysical Research: Atmospheres*,
837 119(6), 3500-3515. https://doi.org/10.1002/2013JD021297